

Fast Evaluation of the Biot-Savart Integral using FFT for Electrical Conductivity Imaging

Hassan Yazdanian^{a,*}, Guilherme B Saturnino^{b,c}, Axel Thielscher^{b,c},
Kim Knudsen^d

^a*Department of Biomedical Engineering, K. N. Toosi University of Technology, Tehran, Iran*

^b*Department of Health Technology, Technical University of Denmark, 2800 Kgs. Lyngby, Denmark*

^c*Danish Research Centre for Magnetic Resonance, Copenhagen University Hospital Hvidovre, Hvidovre, Denmark*

^d*Department of Applied Mathematics and Computer Science, Technical University of Denmark, 2800 Kgs. Lyngby, Denmark*

Abstract

Magnetic resonance electrical impedance tomography (MREIT) and current density imaging (MRCDI) are emerging as new methods to non-invasively assess the electric conductivity of and current density distributions within biological tissue in vivo. The accurate and fast computation of magnetic fields caused by low frequency electrical currents is a central component of the development, evaluation and application of reconstruction methods that underlie the estimations of the conductivity and current density, respectively, from the measured MR data. However, methods for performing these computations have not been well established in the literature. In the current work, we describe a fast and efficient technique to evaluate the Biot-Savart integral based on the fast Fourier transform (FFT), and evaluate its convergence. We show that the method can calculate magnetic fields in realistic human head models in one minute on a standard computer, while keeping error below 2%.

Keywords: Biot-Savart Integral, Conductivity, FFT, Forward problem, Magnetic field

*Corresponding author

Email address: h.yazdanian@ee.kntu.ac.ir (Hassan Yazdanian)

This work was initiated while Hassan Yazdanian was a visiting PhD student at the Department of Applied Mathematics and Computer Sciences in Technical University of Denmark.

1. Introduction

Novel magnetic resonance (MR) methods have been leveraging the high sensitivity of MR to inhomogeneities in the main magnetic field of the scanner to image the electrical impedance of biological tissue at low frequency (MR electric impedance tomography - MREIT)[1, 2] or to assess current density distributions inside the tissue (MR current density imaging - MRCDI)[3, 4]. In these applications, an external current source produces a static or quasi-static *imaging current* inside a body part, and the MR scan is optimized to be sensitive to the magnetic fields produced by these currents. Due to the nature of MR imaging, typically only a single component of the magnetic field can be measured. Therefore, inverse methods are needed to reconstruct the electrical impedance (MREIT) or the current flow (MRCDI) inside the volume conductor from the measurements [5].

The inverse methods typically require the calculation of magnetic fields caused by the externally applied *imaging current* (the forward problem) [3, 6, 7, 8, 9]. This can be done by direct evaluation of the Biot-Savart integral [6, 10, 11], solving a Poisson's equation for magnetic field [10, 11], or using the fast fourier transform (FFT) to compute the Biot-Savart integral [11, 12, 13]. This last method has been shown to be the fastest among the three [11]. Other methods such as Fast multipole method (FMM) can also be applied to efficiently compute the Biot-Savart integral [14], but can be difficult to implement and is generally slower than FFT [15]. However, to the best of our knowledge, the numerical accuracy of the FFT method for the Biot-Savart integral calculations in MREIT and MRCDI forward calculation applications has not been evaluated in detail so far.

In the current work, we describe an FFT-based method for calculating the Biot-Savart integral and assess its speed and accuracy using both phantoms with analytical solutions and a realistic head model. We show that the method performs well in both conditions, being able to produce accurate solutions in

reasonable time, and is therefore a good candidate to compute the magnetic field in forward simulation of MREIT and MRCDI. The method will be integrated in the free and open source software SimNIBS [16], which is currently capable of simulating electrical potential, electrical field, and current density field inside biological tissues, turning it into an integrated tool for MREIT and MRCDI forward calculations.

2. Methods

2.1. Low frequency current-injected bioelectromagnetic phenomena

Assuming the human body to be an ohmic conductor with electrical conductivity $\sigma(\mathbf{x})$, the electric potential $u(\mathbf{x})$ caused by an externally injected low frequency current is governed by the Laplace equation with the Neumann boundary conditions:

$$\begin{aligned}\nabla \cdot (\sigma(\mathbf{x})\nabla u(\mathbf{x})) &= 0 \quad \text{in } \Omega, \\ -\sigma\nabla u \cdot \mathbf{n} &= g \quad \text{on } \partial\Omega,\end{aligned}\tag{1}$$

where the physical body corresponds to a bounded domain $\Omega \subset \mathbb{R}^3$ with a smooth boundary $\partial\Omega$, \mathbf{x} is a position vector in \mathbb{R}^3 , g is the normal current flux through the boundary, and \mathbf{n} is the outward unit normal vector on $\partial\Omega$. A unique solution u for (1) can be obtained by choosing a grounding of the potential, for instance as $u(\mathbf{x}_0) = 0$ for $\mathbf{x}_0 \in \Omega$.

The electric field inside Ω is given by

$$\mathbf{E} = -\nabla u\tag{2}$$

and the current density field inside Ω is given by Ohm's law

$$\mathbf{J} = \sigma\mathbf{E} = -\sigma\nabla u.\tag{3}$$

Outside Ω we have $\mathbf{J} = 0$.

The presence of \mathbf{J} inside Ω gives rise to a magnetic field \mathbf{B} obtained by the Biot-Savart integral

$$\mathbf{B}(\mathbf{x}) = \frac{\mu_0}{4\pi} \int_{\Omega} \mathbf{J}(\mathbf{x}') \times \frac{\mathbf{x} - \mathbf{x}'}{|\mathbf{x} - \mathbf{x}'|^3} d\mathbf{x}',\tag{4}$$

where μ_0 is the magnetic permeability of vacuum. Note that the domain for
45 integration is the bounded set Ω .

In complex geometries such as the ones found in the human body, we must
resort to numerical methods such as the Finite Element Method (FEM) for
computing the electric potential caused by the injected currents, and therefore
of the other quantities derived from it (Eqs. (1)-(4)). There are many readily
50 available open source tools for calculating electric potentials, electric fields and
current density fields in bioelectric applications such as SimNIBS [16], EIDORS
[17], and OpenMEEG [18]. However, the MREIT forward problem is given in
terms of the mapping from σ to \mathbf{B} and the MRCDI forward problem is given by
the mapping $\mathbf{J} \mapsto \mathbf{B}$, and thus both require the evaluation of magnetic fields in
55 large sections of the domain (Eq. (4)), something which is not readily available
in an efficient form in the cited packages.

2.2. Fast Evaluation of the Biot-Savart Integral

Our approach for fast evaluation of the Biot-Savart integral (Eq. (4)) using
FFT is inspired by similar work for a 2D problem [19].

We can rewrite (4) in Cartesian coordinate functions $\mathbf{B} = (B_1, B_2, B_3)$ as a
convolution:

$$\begin{aligned}
B_1(\mathbf{x}) &= \frac{\mu_0}{4\pi} \int_{\Omega} \frac{(x_3 - x'_3)J_2(\mathbf{x}') - (x_2 - x'_2)J_3(\mathbf{x}')}{|\mathbf{x} - \mathbf{x}'|^3} d\mathbf{x}' \\
&= \mu_0(G_3 * J_2 - G_2 * J_3)(\mathbf{x}), \\
B_2(\mathbf{x}) &= \frac{\mu_0}{4\pi} \int_{\Omega} \frac{(x_1 - x'_1)J_3(\mathbf{x}') - (x_3 - x'_3)J_1(\mathbf{x}')}{|\mathbf{x} - \mathbf{x}'|^3} d\mathbf{x}' \\
&= \mu_0(G_1 * J_3 - G_3 * J_1)(\mathbf{x}), \\
B_3(\mathbf{x}) &= \frac{\mu_0}{4\pi} \int_{\Omega} \frac{(x_2 - x'_2)J_1(\mathbf{x}') - (x_1 - x'_1)J_2(\mathbf{x}')}{|\mathbf{x} - \mathbf{x}'|^3} d\mathbf{x}' \\
&= \mu_0(G_2 * J_1 - G_1 * J_2)(\mathbf{x}),
\end{aligned} \tag{5}$$

where

$$G_n = \frac{1}{4\pi} \frac{x_n}{|\mathbf{x}|^3}, \quad n = 1, 2, 3 \tag{6}$$

60 are the Biot-Savart integral kernels and $\mathbf{J} = (J_1, J_2, J_3)$ is the current density field, which has compact support.

The convolutions in (5)

$$C_{n,m}(\mathbf{x}) = \mu_0 G_n(\mathbf{x}) * J_m(\mathbf{x}), \quad n \neq m \quad (7)$$

can be calculated numerically in several ways. Consider we have N sampling points where we have evaluated the current density field and want to calculate the magnetic field in the same set of points. Naïve computation of the convolution has the complexity $\mathcal{O}(N^2)$. However, the computation can be done more efficiently in the frequency domain. Using the Fourier transform \mathcal{F} and the inverse Fourier transform \mathcal{F}^{-1} , we obtain:

$$C_{n,m}(\mathbf{x}) = \mu_0 \mathcal{F}^{-1}\{\mathcal{F}\{G_n\} \cdot \mathcal{F}\{J_m\}\}(\mathbf{x}). \quad (8)$$

In this domain, the computation then has linear complexity, $\mathcal{O}(N)$. The Biot-Savart kernel G_n has an analytical form (details are given in Appendix)

$$\mathcal{F}\{G_n\} = -j \frac{k_n}{|\mathbf{k}|^2}. \quad (9)$$

where $\mathbf{k} = (k_1, k_2, k_3)$ is the spatial frequency in radian per meter and j is the imaginary unity. Using the analytical form of the kernel, in addition to reduce the computation time and memory usage, results in a more accurate
65 representation of the kernel in Fourier space than applying the FFT to the kernel evaluated in the physical domain. The current density field \mathbf{J} does not generally have an analytical form, so we must resort to numerical methods for computing the Fourier transform. The FFT algorithm has a complexity of $\mathcal{O}(N \log(N))$, which means that by performing the calculations using the Fourier domain we
70 are able to reduce complexity from $\mathcal{O}(N^2)$ to $\mathcal{O}(N \log(N))$.

There are, however, a few caveats that need to be addressed in order to properly use the FFT to evaluate (7).

1. \mathbf{J} needs to be sampled on a regularly spaced grid. So, if the original simulations were performed on an irregular grid, they need to be interpolated

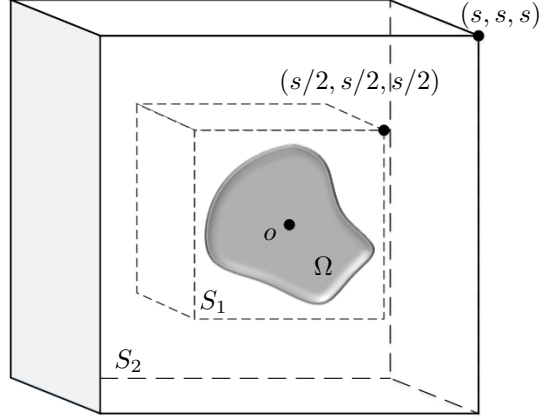


Figure 1: The large cube S_2 determines the periodization of the function. The small cube S_1 shows that the function has compact support. Ω is bounded by the small cube. Both of the cubes are centered at the origin.

75 to obtain a discretized current density field $\bar{\mathbf{J}}$ on an equidistant grid. The resolution of such grid is directly related to the frequency spectra captured by the FFT and therefore the accuracy of the procedure, but also changes the computation time. Therefore, finding an appropriate grid resolution is an important step towards obtaining accurate, yet fast, evaluations of the Biot-Savart integral.

80 2. The FFT calculates a circular convolution, and not the linear convolution required for evaluating (7). However, the linear convolution can be calculated by introducing a *periodization* of the discretized current density field $\bar{\mathbf{J}}$ [20]. Since the current density field is compactly supported in the domain Ω , we define a cube $S_1 = (-s/2, s/2)^3$ in \mathbb{R}^3 centered at the origin o as the *physical domain*, such that $\Omega \subset S_1$. Then, for $\mathbf{x} \in S_1$, the integral (7) only involves values of G_n on the *computational domain* S_2 , where $S_2 = (-s, s)^3$ is a domain with double size of S_1 centered at the origin. Thus, to compute the discrete linear convolution by FFT, we should calculate the FFT of $\bar{\mathbf{J}}$ in S_2 , where the values for $\bar{\mathbf{J}} \notin \Omega$ are set to zero. The result of this operation for $\mathbf{x} \in S_1$, will be identical to the linear convolution. See Fig. 1 for a description of the domains defined above.

After the two steps above are taken into account, we obtain the following equation for calculating the discrete convolution values $\bar{C}_{n,m}$ inside S_2 :

$$\bar{C}_{n,m} = \mu_0 \text{iFFT}(\overline{\mathcal{F}\{G_n\}} \cdot \text{FFT}(\bar{J}_m)). \quad (10)$$

where $\overline{\mathcal{F}\{G_n\}}$ is the analytical Fourier transform (9) evaluated at the spatial frequencies \mathbf{k} present in the FFT transformation. In order to avoid the singularity at $\mathbf{k} = \mathbf{0}$, we set

$$\overline{\mathcal{F}\{G_i\}}[\mathbf{k} = 0] = 0. \quad (11)$$

3. Numerical Experiments

In this section we present some numerical examples for the evaluation of the
95 developed technique. In the first examples we have an analytic expression of the fields \mathbf{J} and \mathbf{B} , and in the final example we used a current density field calculated on a realistic head model using SimNIBS.

3.1. Benchmark tests

In this section we employ two benchmark tests in order to validate the tech-
100 nique developed to compute the Biot-Savart integral. In both tests the magnetic flux density is known analytically, and therefore the performance of the numerical algorithm can be compared to a ground truth. The first example is a smooth phantom, while the second phantom is piecewise smooth.

We start with an explicit magnetic vector potential $\mathbf{A}(\mathbf{x}) = (A_1(\mathbf{x}), A_2(\mathbf{x}),$
105 $A_3(\mathbf{x}))$, which in the ball $B(0, h)$ is given analytically, and outside is set to 0. We then calculate the magnetic field by $\mathbf{B} = \nabla \times \mathbf{A}$. In this way, we obtain a divergence-free magnetic field \mathbf{B} , needed for consistency with Gauss's law for magnetism ($\nabla \cdot \mathbf{B} = 0$). We further calculate the current density field \mathbf{J} by $\nabla \times \nabla \times \mathbf{A} = \mathbf{J}$ which is obtained by using Ampere's law, $\nabla \times \mathbf{B} = \mu \mathbf{J}$, assuming
110 $\mu = 1$ for simplicity.

We consider two different functions \mathbf{A} , both divergence-free. The first \mathbf{A} has a continuous second derivative everywhere and therefore leads to a smooth \mathbf{J} ,

and was defined as

$$\begin{aligned} A_1(\mathbf{x}) &= x_2 x_3 \exp\left(\frac{-1}{h^2 - |\mathbf{x}|^2}\right), \\ A_2(\mathbf{x}) &= x_1 x_3 \exp\left(\frac{-1}{h^2 - |\mathbf{x}|^2}\right), \\ A_3(\mathbf{x}) &= -2x_1 x_2 \exp\left(\frac{-1}{h^2 - |\mathbf{x}|^2}\right). \end{aligned}$$

Generally, however, the solutions for the Laplace equation with Neumann boundary conditions (Eq. (1)) produces values of \mathbf{J} which can be discontinuous on the boundary $\partial\Omega$ and where there are discontinuities in the conductivity $\sigma(\mathbf{x})$. As the Fourier components of discontinuous function fall off slowly and we can only compute truncated terms of the Fourier transform, we need to evaluate how the smoothness of \mathbf{J} affects the convergence of our computations. Therefore, we also used a second \mathbf{A} which has a discontinuous second derivative and therefore a discontinuous \mathbf{J} in the outer boundary $|\mathbf{x}| = h$. It was defined as

$$\begin{aligned} A_1(\mathbf{x}) &= x_2(h - |\mathbf{x}|)^2 \\ A_2(\mathbf{x}) &= x_3(h - |\mathbf{x}|)^2 \\ A_3(\mathbf{x}) &= x_1(h - |\mathbf{x}|)^2. \end{aligned}$$

We used both phantoms to evaluate the FFT method by calculating $\bar{\mathbf{B}}$ numerically based on analytical calculations of the current field density \mathbf{J} . We set $h = 1$, the computational domain had a size $s = 2$ and was discretized using $M = 32, 64, 128, 256$, and 512 equally spaced voxels along each dimensions.

115 3.2. Real head model and simulation setup

We use SimNIBS to simulate a current density field in a realistic situation. The performance of SimNIBS for calculating u and \mathbf{J} has been previously validated in [21].

120 The realistic simulation was run on a head model of a healthy volunteer from the SimNIBS example dataset (www.simnibs.org). For more information

regarding the generation of the head model, please see [22]. This model is a tetrahedral head mesh with $\approx 7 \times 10^5$ nodes and $\approx 5 \times 10^6$ tetrahedral elements segmented into six tissue types: white matter, gray matter, cerebrospinal fluid, skull, scalp and eyes, with conductivities of 0.126 S/m, 0.275 S/m, 1.645 S/m, 0.01 S/m, 0.465 S/m and 0.5 S/m respectively [23].

We used SimNIBS to model two single layer rectangular electrodes of $50mm \times 50mm \times 4mm$ and used them to deliver deliver a 1 mA current. The anode was placed above the C6 position and the cathode above the C5 position according to the EEG 10-20 system. For each electrode, the complete upper surface was set to a common electric potential, corresponding to a highly conductive top layer to distribute the currents[24]. The conductivity of the electrode bodies was set to 1 S/m. [24].

All simulations were implemented in Python 2.7 and the MKL-linked *numpy* package was used for the FFT evaluations. The code was executed on a core i7 3.6 GHz desktop computer with 16 GB RAM.

4. Results and Discussion

4.1. Benchmark tests

Fig. 2 shows slices of the B_3 field calculated analytically and numerically, as well as the errors in the smooth phantom, while Fig. 3 shows the same quantities for the piecewise smooth phantom. We have chosen to display B_3 because some MREIT and MRCDI methods are only sensitive to a single component of the magnetic field, usually denoted B_z or B_3 [25, 26, 4]. Fig. 2a and Fig. 3a depict the analytical B_3 corresponding to smooth and piecewise smooth phantoms, respectively. As can be seen, by increasing the number of grid points from $M = 128$ in Fig. 2b and Fig. 3b to $M = 512$ in Fig. 2c and Fig. 3c, the quality of the computed field is improved. By increasing M , the error in \bar{B}_3 dramatically decreases in both the central region and near the boundary region of the smooth phantom (Fig. 2d and Fig. 2e). As expected, the error for the piecewise smooth phantom decreases much slower than the error for the

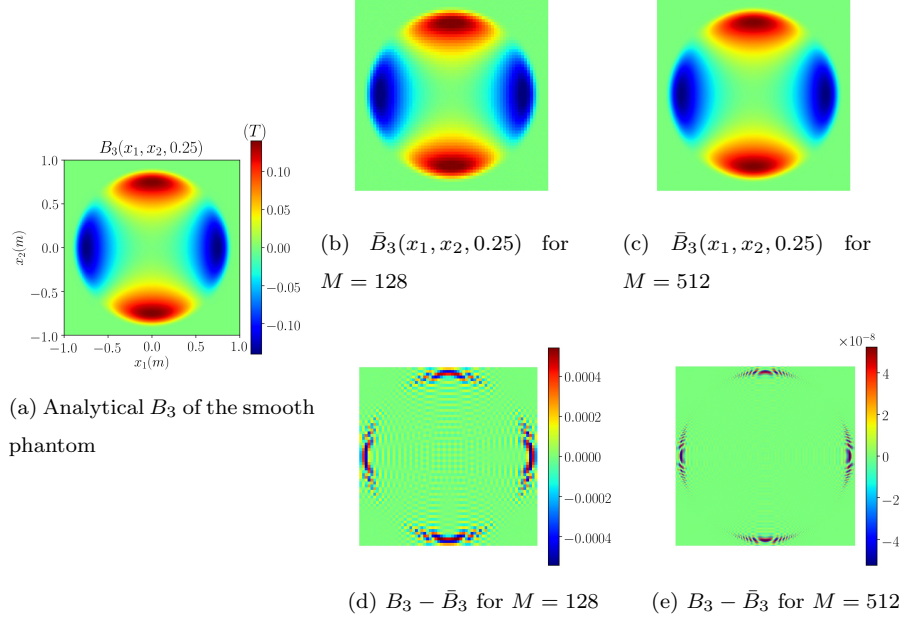


Figure 2: (a) Slice ($x_3 = 0.25$) of the analytical B_3 corresponding to the smooth phantom at $x_3 = 0.25$. Numerical results for \bar{B}_3 for (b) $M = 128$ and (c) $M = 512$. (d) and (e) are the difference images between B_3 and \hat{B}_3 for $M = 128$ and $M = 512$, respectively.

smooth phantom, especially close to the discontinuous outer boundary (Fig. 3d and Fig. 3e). This arises from the piecewise nature of \mathbf{J} which causes the Fourier transform to decay slowly. Thus, truncation of the Fourier transform slows down the convergence rate.

To illustrate the superiority of the FFT-based method over the direct discretization of the Biot-Savart integral, we also numerically evaluated (5) using Simpson's rule. Fig. 4a compares the error of the FFT-based and the numerical integration methods for the benchmark tests. The lines depict the relative error of \mathbf{B} versus the number of grid points along each axis M in the computational domain. It is worth to mention that in the comparison in Fig. 4 we have the $M = 16, 32, \dots$ corresponding to $N = 8, 16, \dots$ in the physical domain for the numerical integration. The blue line with left triangles and the red line with right triangles are errors for smooth and piecewise smooth phantoms, respec-

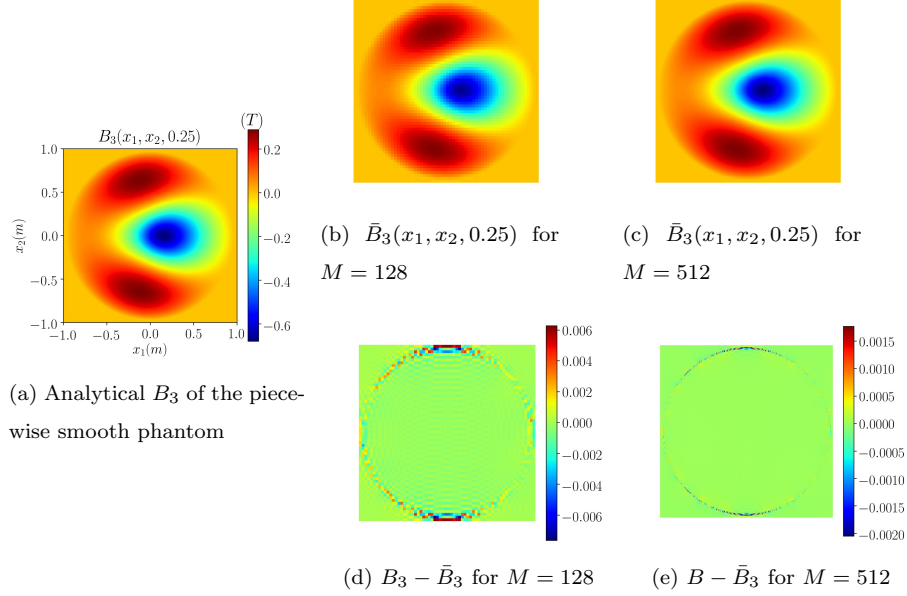


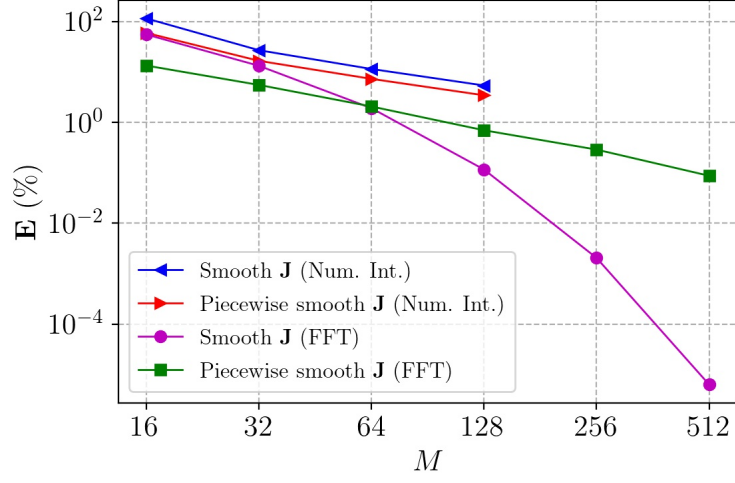
Figure 3: (a) Slice ($x_3 = 0.25$) of the analytical B_3 corresponding to the piecewise smooth phantom at $x_3 = 0.25$. Numerical results for \bar{B}_3 for (b) $M = 128$ and (c) $M = 512$. (d) and (e) are the difference images between B_3 and \bar{B}_3 for $M = 128$ and $M = 512$, respectively.

tively, when the numerical integration method was used. Since the computation time was too high, the error was calculated for only four M in this method. The magenta line with circles and the green line with squares are errors for smooth and piecewise smooth phantoms, respectively, when the FFT-based method was used. The error was calculated by:

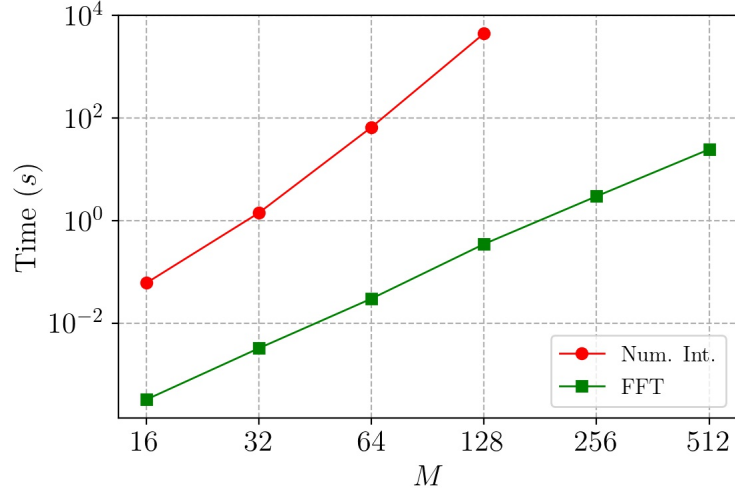
$$\mathbf{E}(\%) = 100 \times \frac{\|\mathbf{B} - \bar{\mathbf{B}}\|}{\|\mathbf{B}\|} \quad (12)$$

where $\mathbf{B} = (B_1, B_2, B_3)$ and $\bar{\mathbf{B}} = (\bar{B}_1, \bar{B}_2, \bar{B}_3)$ are the analytical and numerical magnetic field, respectively, and $\|\cdot\|$ denotes the L_2 -norm calculated in the discrete domain.

As can be seen from Fig. 4a, the results are converging for both tests and for both methods. The convergence rate for the numerical integration method with both continuous and discontinuous \mathbf{J} is approximately the same, as it does not suffer from the discontinuity-induced artifacts as the FFT method



(a) FFT-based method vs Numerical integration



(b) Computation time for numerical integration and FFT-based method

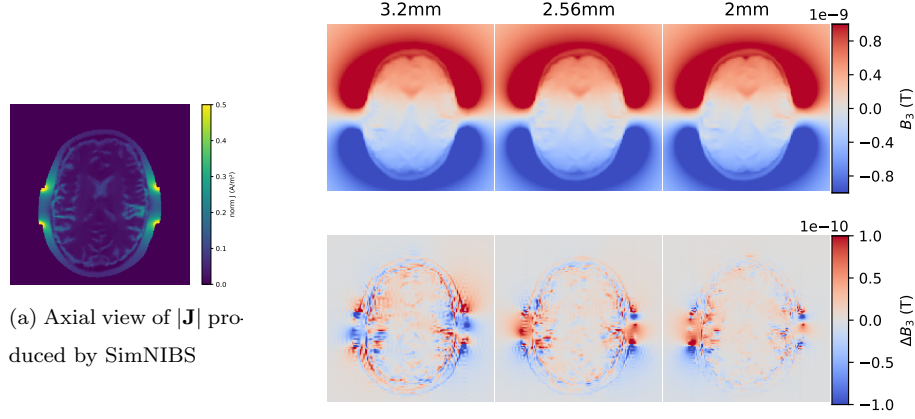
Figure 4: (a) Relative error of \mathbf{B} versus number of grid points along each axis (M) using smooth \mathbf{J} and numerical integration (blue line with left triangles), piecewise smooth \mathbf{J} and numerical integration (red line with right triangles), smooth \mathbf{J} and FFT-based method (magenta line with circles), and piecewise smooth \mathbf{J} and FFT-based method (green line with squares). (b) Computation time for numerical integration (blue line with circles) and FFT-based method (red line with squares) versus M .

does. However, the convergence rate is different for the FFT-based method with each phantom. It can be said that convergence rate and smoothness are inversely related for the FFT-based method. For $M = 64$, the errors of the FFT-based method are more than three times lower than those of the numerical
165 integration for both phantoms. With regard to the constant convergence rate of the numerical integration method, it can be predicted that for larger M , this method produces larger errors than the FFT approach. For $M = 512$, the error for the smooth \mathbf{J} was below $5 \times 10^{-8} \%$ and for the piecewise smooth \mathbf{J} was below 0.5% in the FFT-based method.

170 Fig. 4b shows the computation time for each method. The red line with circles and the green line with squares are the elapsed time for the numerical integration and FFT-based methods, respectively, versus different M . We can see that direct numerical computation of the Biot-Savart integral is much more time consuming than the FFT approach. For $M = 64$ ($M^3 = 262,144$, total
175 number of grid points in the computational domain), the computation time of direct numerical method was around 4405 seconds. This is while, for $M = 512$ ($M^3 = 134,217,728$), the computation time of FFT-based method was less than 25 seconds.

Table 1: Voxel sizes and corresponding number of grid points for calculation on the realistic head model

Voxel size (mm ³)	M	M^3
3.2	160	4,096,000
2.56	200	8,000,000
2	256	16,777,216
1.6	320	32,768,000
1	512	134,217,728
0.5 (Ground-truth)	1,024	1,073,741,824



(a) Axial view of $|\mathbf{J}|$ produced by SimNIBS

(b) Third component of magnetic field B_3 and its error ΔB_3

Figure 5: Results of the realistic simulation. (a) Axial view of $|\mathbf{J}|$ produced by SimNIBS, plotted at 1mm resolution. (b) (First row) Third component of the magnetic field for voxel sizes of 3.2 mm^3 (first column), 2 mm^3 (second column) and 1 mm^3 (third column). (Second row) Corresponding error with relation to the B_3 field computed at a high resolution (0.5 mm^3)

4.2. Realistic simulation

Fig. 5a shows the distribution of the norm of the current density field, $|\mathbf{J}|$, in an axial slice of the realistic head model. The first row of Fig. 5b displays the corresponding B_3 in the same slice and for different voxel sizes. The second row of Fig. 5b depicts the error in the computed B_3 for each voxel size compared to the magnetic field computed at a high resolution with a voxel size of 0.5 mm^3 . As can be seen, the error decreases by increasing the resolution. In addition, as we expected, the maximum error occurred near the place of electrodes due to discontinuity in the current density field.

To compute \mathbf{B} by FFT-based methods, it is required to convert \mathbf{J} defined on the elements of the tetrahedral mesh to the points of the defined regular grid. This was done using the `interpolate_to_grid` function in SimNIBS, which grids the data using the superconvergent patch recovery (SPR)-based

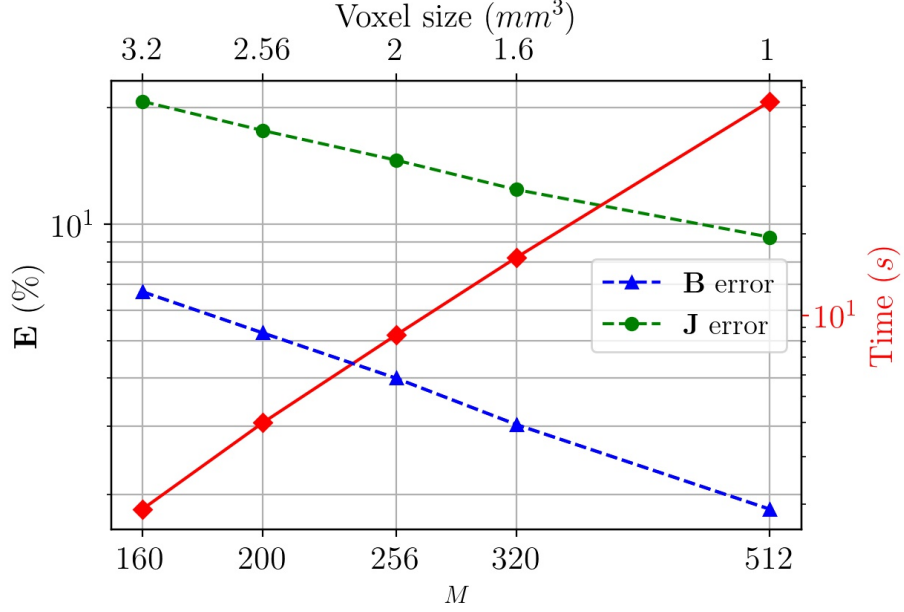


Figure 6: Relative error versus M using the first approach (blue dashed line) and the second approach (green dashed line). The red line is computation time versus M .

interpolation described in [21]. The computation time for this function was approximately 40 seconds for all field resolutions, as there is a high overhead (the nodal recovery process) associated with the gridding at all resolutions.

195 To evaluate the FFT-based method in the realistic simulation situation, we considered two approaches:

1. First, we tried different voxel sizes to see how the method converges by decreasing the voxel size (Table 1). In this approach, we considered the voxel size of $0.5mm \times 0.5mm \times 0.5mm$ as a ground-truth and calculated the error of magnetic field using (12). To compare the magnetic field at each resolution with the ground-truth, we resampled the low resolution data to the high resolution data using an spline interpolation of order 3. It is worthwhile mentioning this step could result in interpolation errors.
2. In the second approach, we used a back-and-forth procedure. We computed the magnetic field using the FFT-based method for the current

density field produced by SimNIBS, \mathbf{J}_{sim} . Then, using Ampere's law, we reproduced the current density distribution by numerically applying the curl operator to the computed magnetic field. However, the curl of a vector field is solenoidal (divergence free) whereas the initial \mathbf{J}_{sim} is non-solenoidal due to the discontinuity at the electrode surfaces. To resolve this problem, we used the Helmholtz decomposition [27] to compute the solenoidal part of \mathbf{J}_{sim} , \mathbf{J}_{so} . Based on the Helmholtz decomposition we can write $\mathbf{J}_{so} = \mathbf{J}_{sim} - \mathbf{J}_{ir}$, where \mathbf{J}_{ir} is the irrotational (curl free) part of \mathbf{J}_{sim} . We calculated \mathbf{J}_{ir} in the frequency domain as follows [27]

$$\mathcal{F}\{\mathbf{J}_{ir}\} = \mathbf{k} \frac{\mathbf{k} \cdot \mathcal{F}\{\mathbf{J}_{sim}\}}{|\mathbf{k}|^2}. \quad (13)$$

Then, we subtracted (13) from $\mathcal{F}\{\mathbf{J}_{sim}\}$ to obtain the Fourier transform of \mathbf{J}_{so} . By applying $\mathcal{F}^{-1}\{\cdot\}$ to the result, we obtained an approximation of \mathbf{J}_{so} . Finally, we considered the resultant field as the input of the back-and-forth procedure. To calculate the curl, we used the central finite difference.

For both approaches, we considered a computation domain of size $512mm \times 512mm \times 512mm$, enough to encompass the entire head and the periodization of the domain.

Fig. 6 shows the results for both approaches. The blue dashed line with triangles is the error of magnetic field in the first approach and the green dashed line with dots is the error of current density field in the second one. As can be seen from Fig. 6, the results are converging for both approaches. Furthermore, the convergence rates are approximately the same. However, the error values for the second approach are higher. We believe this is because of the error arising from the additional numerical differentiation performed in the back-and-fourth procedure.

The red line with squares in Fig. 6 show the computation time of magnetic field \mathbf{B} for different voxel sizes. The elapsed time for a voxel size of 0.5 mm^3 was about 1 minute while the maximum memory usage in this resolution was 12.3 GB. For a voxel size of 2 mm^3 these amounts decrease dramatically to a

computation time of 8.5 seconds and a memory usage of 181 MB, and we are
 225 able to obtain results whose numerical accuracy in brain tissue is around one
 order of magnitude better than the current MRCDI measurement methods [4],
 and thus could be suited for some conductivity reconstruction algorithms.

5. Conclusion

In this paper, we developed a computationally efficient technique for evalua-
 230 tion of the Biot-Savart integral. This integral has the form of a convolution, and
 thus lends itself well to an efficient numerical evaluation by means of the FFT al-
 gorithm. We performed three numerical experiments to evaluate the technique,
 using two phantoms with known analytical solutions and in addition a realistic
 head model. The results show a good convergence in all three experiments,
 235 suggesting that the method is appropriate to, for example, forward modelling
 of MREIT and MRCDI applications. These modalities measure only one com-
 ponent of the magnetic field. It is straightforward to use the suggested method
 for only calculating the required component, which results in a further roughly
 threefold increase in speed while decreasing memory consumption threefold.

240 By integrating this new feature in SimNIBS, a fast and comprehensive pack-
 age for modeling of low frequency exogenic bioelectromagnetic phenomena is
 available. It can compute the electrical potential u , current density field \mathbf{J} , and
 magnetic field \mathbf{B} in a realistic head domain with typical pixel sizes in less than
 three minutes. This opens the door for the development of new methods for
 245 current and tissue conductivity reconstruction from imaging and tomography
 data based on low-frequency electromagnetics, such as MREIT and MRCDI.

We can obtain further improvement for this technique by using DSP tech-
 niques such as FFTW [28] to decrease the computation time or overlap add/save
 methods [29] to save memory.

250 Appendix: Fourier transform of the Biot-Savart kernel

In this section the details for extraction of (9) are presented. Applying the Fourier transform to G_i yields

$$\begin{aligned}\mathcal{F}\{G_i\} &= \mathcal{F}\left\{\frac{1}{4\pi} \frac{x_i}{|\mathbf{x}|^3}\right\} \\ &= \mathcal{F}\left\{-\frac{\partial}{\partial x_i} \frac{1}{4\pi|\mathbf{x}|}\right\} \\ &= -jk_i \mathcal{F}\left\{\frac{1}{4\pi|\mathbf{x}|}\right\}.\end{aligned}\tag{A1}$$

Now $1/4\pi|\mathbf{x}|$ is the fundamental solution for the negative Laplace operator and its Fourier transform is given by [30]

$$\mathcal{F}\left\{\frac{1}{4\pi|\mathbf{x}|}\right\} = \frac{1}{|\mathbf{k}|^2}.\tag{A2}$$

By substituting (A2) into (A1), we obtain (9):

$$\mathcal{F}\{G_i\} = -\frac{jk_i}{|\mathbf{k}|^2}.\tag{A3}$$

References

- [1] J. K. Seo, E. J. Woo, Electrical tissue property imaging at low frequency using MREIT, IEEE Transactions on Biomedical Engineering 61 (5) (2014) 1390–1399.
- 255 [2] Y. Song, H. Ammari, J. K. Seo, Fast magnetic resonance electrical impedance tomography with highly undersampled data, SIAM Journal on Imaging Sciences 10 (2) (2017) 558–577.
- [3] O. I. Kwon, S. Z. Sajib, I. Sersa, T. I. Oh, W. C. Jeong, H. J. Kim, E. J. Woo, Current density imaging during transcranial direct current stimulation using DT-MRI and MREIT: algorithm development and numerical
260 simulations, IEEE Transactions on Biomedical Engineering 63 (1) (2015) 168–175.

- [4] C. Göksu, L. G. Hanson, H. R. Siebner, P. Ehses, K. Scheffler, A. Thielscher, Human in-vivo brain magnetic resonance current density imaging (MRCDI), *NeuroImage* 171 (2018) 26–39.
- [5] C. Park, B. I. Lee, O. I. Kwon, Analysis of recoverable current from one component of magnetic flux density in MREIT and MRCDI, *Physics in Medicine & Biology* 52 (11) (2007) 3001.
- [6] Y. Z. Ider, S. Onart, Algebraic reconstruction for 3D magnetic resonance-electrical impedance tomography (MREIT) using one component of magnetic flux density, *Physiological Measurement* 25 (1) (2004) 281.
- [7] M. Chauhan, A. Indahlastari, A. K. Kasinadhuni, M. Schär, T. H. Mareci, R. J. Sadleir, Low-frequency conductivity tensor imaging of the human head in vivo using DT-MREIT: First study, *IEEE Transactions on Medical Imaging* 37 (4) (2017) 966–976.
- [8] Z. J. Meng, S. Z. Sajib, M. Chauhan, R. J. Sadleir, H. J. Kim, O. I. Kwon, E. J. Woo, Numerical simulations of MREIT conductivity imaging for brain tumor detection, *Computational and Mathematical Methods in Medicine* 2013.
- [9] S. Z. Sajib, N. Katoch, H. J. Kim, O. I. Kwon, E. J. Woo, Software toolbox for low-frequency conductivity and current density imaging using MRI, *IEEE Transactions on Biomedical Engineering* 64 (11) (2017) 2505–2514.
- [10] B. I. Lee, S. H. Oh, E. J. Woo, S. Y. Lee, M. H. Cho, O. Kwon, J. K. Seo, J.-Y. Lee, W. S. Baek, Three-dimensional forward solver and its performance analysis for magnetic resonance electrical impedance tomography (MREIT) using recessed electrodes, *Physics in Medicine & Biology* 48 (13) (2003) 1971.
- [11] A. S. Minhas, H. H. Kim, Z. J. Meng, Y. T. Kim, H. J. Kim, E. J. Woo, Three-dimensional MREIT simulator of static bioelectromagnetism and MRI, *Biomedical Engineering Letters* 1 (2) (2011) 129–136.

- [12] B. L. Schwartz, M. Chauhan, R. J. Sadleir, Analytic modeling of conductively anisotropic neural tissue, *Journal of Applied Physics* 124 (6) (2018) 064701.
- [13] A. Antal, M. Bikson, A. Datta, B. Lafon, P. Dechent, L. C. Parra, W. Paulus, Imaging artifacts induced by electrical stimulation during conventional fMRI of the brain, *Neuroimage* 85 (2014) 1040–1047.
- [14] A. Adedoyin, P. Andrei, 3D magnetostatic using the fast multiple method, *IEEE Transactions on Magnetics* 43 (6) (2007) 2914–2916.
- [15] J. P. Boyd, Multipole expansions and pseudospectral cardinal functions: A new generalization of the fast Fourier transform, *Journal of Computational Physics* 103 (1) (1992) 184–186.
- [16] A. Thielscher, A. Antunes, G. B. Saturnino, Field modeling for transcranial magnetic stimulation: a useful tool to understand the physiological effects of TMS?, in: 2015 37th annual international conference of the IEEE engineering in medicine and biology society (EMBC), IEEE, 2015, pp. 222–225.
- [17] A. Adler, W. R. Lionheart, Uses and abuses of EIDORS: an extensible software base for EIT, *Physiological Measurement* 27 (5) (2006) S25.
- [18] A. Gramfort, T. Papadopoulo, E. Olivi, M. Clerc, OpenMEEG: open source software for quasistatic bioelectromagnetics, *Biomedical Engineering Online* 9 (1) (2010) 45.
- [19] K. Knudsen, J. Mueller, S. Siltanen, Numerical solution method for the dbar-equation in the plane, *Journal of Computational Physics* 198 (2) (2004) 500–517.
- [20] R. Priemer, *Introductory signal processing*, Vol. 6, World Scientific Publishing Company, 1990.
- [21] G. B. Saturnino, K. H. Madsen, A. Thielscher, Electric field simulations for transcranial brain stimulation using FEM: an efficient implementation and error analysis, *Journal of Neural Engineering*: in press.

- [22] J. D. Nielsen, K. H. Madsen, O. Puonti, H. R. Siebner, C. Bauer, C. G. Madsen, G. B. Saturnino, A. Thielscher, Automatic skull segmentation from MR images for realistic volume conductor models of the head: Assessment of the state-of-the-art, *Neuroimage* 174 (2018) 587–598.
- [23] M. Windhoff, A. Opitz, A. Thielscher, Electric field calculations in brain stimulation based on finite elements: an optimized processing pipeline for the generation and usage of accurate individual head models, *Human Brain Mapping* 34 (4) (2013) 923–935.
- [24] G. B. Saturnino, A. Antunes, A. Thielscher, On the importance of electrode parameters for shaping electric field patterns generated by tDCS, *Neuroimage* 120 (2015) 25–35.
- [25] J. K. Seo, J. R. Yoon, E. J. Woo, O. Kwon, Reconstruction of conductivity and current density images using only one component of magnetic field measurements, *IEEE Transactions on Biomedical Engineering* 50 (9) (2003) 1121–1124.
- [26] C. Park, O. Kwon, E. J. Woo, J. K. Seo, Electrical conductivity imaging using gradient B_z decomposition algorithm in magnetic resonance electrical impedance tomography (MREIT), *IEEE Transactions on Medical Imaging* 23 (3) (2004) 388–394.
- [27] A. J. Devaney, Mathematical foundations of imaging, tomography and wavefield inversion, Cambridge University Press, 2012, Ch. The electromagnetic field, pp. 461–463.
- [28] M. Frigo, S. G. Johnson, The design and implementation of FFTW3, *Proceedings of the IEEE* 93 (2) (2005) 216–231.
- [29] A. V. Oppenheim, R. W. Schaffer, Discrete-Time Signal Processing, 3rd Edition, Prentice Hall Press, Upper Saddle River, NJ, USA, 2009.
- [30] P. Kythe, Fundamental solutions for differential operators and applications, Springer Science & Business Media, 2012.